Imaging-based molecular barcoding with pixelated dielectric metasurfaces

Andreas Tittl[1], Aleksandrs Leitis[1], Mingkai Liu[2], Filiz Yesilkoy[1], Duk-Yong Choi[3], Dragomir N. Neshev[2], Yuri S. Kivshar[2], and Hatice Altug[1*]

[1]Institute of BioEngineering, École Polytechnique Fédérale de Lausanne (EPFL), Lausanne 1015, Switzerland

[2]Nonlinear Physics Centre, Research School of Physics and Engineering, Australian National University, Canberra, ACT 2601, Australia.

[3]Laser Physics Centre, Research School of Physics and Engineering, Australian National University, Canberra, ACT 2601, Australia.

*Correspondence to: hatice.altug@epfl.ch

Abstract:

Metasurfaces provide opportunities for wavefront control, flat optics and sub-wavelength light concentration. We introduce an imaging-based nanophotonic method for detecting mid-infrared molecular fingerprints, and implement it for the chemical identification and compositional analysis of surface-bound analytes. Our technique leverages a two-dimensional pixelated dielectric metasurface featuring a range of ultra-sharp resonances each tuned to discrete frequencies, enabling molecular absorption signatures to be read out at multiple spectral points and this information to be translated into a barcode-like spatial absorption map for imaging. The signatures of biological, polymer, and pesticide molecules can be detected with high sensitivity, covering applications ranging from biosensing to environmental monitoring. Our chemically specific technique is capable of resolving absorption fingerprints without the need for spectrometry, frequency scanning, or moving mechanical parts, redefining the boundaries of surface-enhanced molecular detection and paving the way towards sensitive and versatile miniaturized mid-infrared spectroscopy devices.

Main text:

The mid-infrared (mid-IR) spectrum is essential for sensing due to the presence of characteristic molecular absorption fingerprints originating from the intrinsic vibrational modes of chemical bonds. Mid-IR spectroscopy is widely recognized as the gold standard for chemical analysis, because it allows a direct characterization of molecular structures with chemical specificity unique to this spectral range (*1*). It is also a powerful nondestructive and label-free technique for identifying biochemical building blocks, including proteins, lipids, and DNA, among others. However, due to the mismatch between mid-IR wavelengths and dimensions of molecules, the sensitivity of mid-IR spectroscopy is limited when detecting signals from nanometer-scale samples (*2*), biological membranes (*3*), or low numbers of surface-bound molecules (*4*).

Nanophotonics can overcome this limitation by exploiting the strong near-field enhancement of subwavelength resonators. When the resonance is spectrally overlapped with the absorption fingerprints, the enhanced molecule-resonator coupling can lead to a change in either

the frequency or the strength of the resonance, from which the molecular fingerprints can be extracted. This concept, surface-enhanced infrared absorption (SEIRA), has been realized using various plasmonic platforms (*5*–*7*); however, the achieved performance is still far from ideal due to the inherent limitation of low quality factor (Q-factor) resonances imposed by resistive loss. Recently, nanostructured resonators based on high-index dielectric materials have emerged as building blocks for various metadevices due to their low intrinsic loss and CMOS compatibility, demonstrating capabilities for controlling the propagation and localization of light (*8*, *9*). Many applications including generalized wave front control (*10*, *11*), ultra-thin optical elements (*12*, *13*), and antenna-based light concentration (*14*) have been shown experimentally. A key concept underlying the functionalities of many metasurface approaches is their use of constituent elements with spatially varying optical properties. The full potential of metasurface-based SEIRA with both spectral and spatial control over the nanoscale field enhancement has yet to be realized.

We report a mid-IR nanophotonic sensor based on all-dielectric high-Q metasurface elements and demonstrate its capability for enhancing, detecting, and differentiating the absorption fingerprints of various molecules. Traditionally, high-Q resonances in metasurfaces are generated via the interference of super-radiant and sub-radiant modes (*15*–*17*). In contrast, our design exploits the collective behavior of Mie resonances, which can be recognized as supercavity modes driven by the physics of bound states in the continuum (*18*). Furthermore, the high-Q resonances of our design are spectrally clean without additional resonance background, which is particularly attractive because it allows for the highly spectrally selective enhancement of spectroscopically rich molecular fingerprint information. Specifically, we implement a two dimensional (2D) array of high-Q metasurface pixels, where the resonance positions of individual metapixels are linearly varied over a target mid-IR fingerprint range. This configuration allows us to assign each resonance position to a specific pixel of the metasurface, establishing a one-to-one mapping between spectral and spatial information (Fig. 1A). By comparing the imaging-based readout of this spatially encoded vibrational information before and after the coating of target analyte molecules, we demonstrate chemically specific molecular barcodes suitable for chemical identification and compositional analysis.

Individual metapixels contain a zig-zag array of anisotropic hydrogenated amorphous silicon (a-Si:H) resonators, which provide high-Q resonances when excited with linearly polarized light and allow for straightforward resonance tuning via scaling of its geometrical parameters by a factor S (Fig. 1B). Numerically simulated reflectance spectra of an exemplary 5 x 5 metasurface pixel array with a scaling factor variation from S = 1.0 to S = 1.3 show sharp resonance peaks (average Q > 200) with near-unity reflectance intensity and linear tunability of the resonance positions covering the spectral range from 1350 cm^{-1} to 1750 cm^{-1} (Fig. 1C). Our metapixel design also provides more than three orders of magnitude enhancement of the local electric near-field intensity confined to the resonator surface (*19*), which is ideal for the sensitive detection of analyte molecular vibrations (Fig. 1D, Fig. S1). The target spectral range from 1350 cm^{-1} to 1750 cm^{-1} contains characteristic molecular stretching/bending vibrations found in hydrocarbons and amino acids, making it crucial for detecting and differentiating the absorption signatures of biomolecules, environmental pollutants, and polymeric species, among others. We first focus on a biosensing application by showing chemical-specific protein detection, where the distinct protein absorption fingerprint is governed by the amide I and II vibrational bands located at around 1660 cm^{-1} and 1550 cm^{-1}, respectively.

A sub-5 nm conformal protein layer covering the pixelated metasurface causes a pronounced modulation of the individual metapixel reflectance spectra due to the coupling between the molecular vibrations and the enhanced electric near-fields around the dielectric resonators. This reflectance modulation manifests primarily as an attenuation and broadening of the metapixel resonance, which are correlated with the strength of the amide I and II molecular vibrations (Fig. 1E). The envelope of the metapixel reflectance spectra unambiguously reproduces the protein absorption signature, confirming efficient molecular fingerprint detection. The metapixel resonances provide linewidths much narrower than the spectral feature size of the individual amide I and II absorption bands at around 60 cm^{-1}. This is in strong contrast to metal-based antennas used in plasmonic SEIRA approaches, which typically exhibit linewidths above 200 cm^{-1} limited by the intrinsic damping of the metal (*5*). This advantage allows us to read out the protein absorption signature at multiple discrete frequency points and to translate this spectrally resolved absorption information into a barcode-like spatial map of the individual metapixel absorption signals (Fig. 1F).

A pixelated dielectric metasurface design consisting of an array of 10 x 10 metapixels was fabricated using electron-beam lithography and reactive ion beam etching. Ellipse axes and unit cell periodicities are identical to the values given for the numerical simulations in Fig. 1 and the unit cell was linearly scaled between S = 1.00 and S = 1.34 in 100 steps. A fixed metapixel size of 100 µm x 100 µm was chosen to provide a trade-off between metapixel signal-to-noise ratio and number of pixels (Fig. 2A, Fig. S2). Analysis of scanning electron microscopy (SEM) images captured for multiple metapixels confirms the accurate reproduction of the resonator design as well as the linear scaling of the unit cell geometry over the entire metasurface area (Fig. 2B, Fig. S3).

The metasurface is characterized in reflection using a quantum cascade laser-based mid-IR microscope equipped with a 480 x 480 pixel array-based imaging detector. We utilize a refractive 4X objective with a 2 mm field of view (FOV) to acquire the optical response of all metasurface pixels simultaneously (Fig. 2C). Reflectance images captured for different wavenumbers of the incident mid-IR radiation are shown in Fig. 2D. At each incident wavenumber, high reflectance intensity indicates the excitation of a metapixel with matching resonance frequency in a specific spatial location on the metasurface. Reflectance spectra are obtained by combining reflectance images for a range of incident wavenumbers and integrating the resulting spectrally resolved data over the individual metapixel areas (see Methods). The spectra of 21 exemplary metapixels and extracted resonance positions of all 100 metasurface pixels are shown in Fig. 2E and Fig. 2F. The fabricated pixelated metasurface delivers resonances with low average full width at half maximum (FWHM) of 13.7 cm^{-1} and uniform tuning of the resonance frequency over the amide band range from 1370 cm^{-1} to 1770 cm^{-1}. This corresponds to a spectral resolution of 4 cm^{-1} and an average Q-factor of 115 (Fig. S4), which is an improvement of more than one order of magnitude over metallic antenna geometries (*20*, *21*). Importantly, our design can easily be extended to cover a larger spectral region by increasing the range of geometrical scaling parameters (Fig. S5).

We demonstrate molecular fingerprint detection by interrogating a physisorbed monolayer of recombinant protein A/G. Metapixel reflectance spectra before and after the protein A/G physisorption are presented in Figs. 3A and 3B, respectively. All spectra are normalized to the peak reflectance values of the reference measurement without analyte. The absorbance signal calculated from the peak reflectance envelopes before (R_0) and after physisorption (R_S) reveals the characteristic amide I and II absorption signature of the protein A/G molecules, which is in good

agreement with an independent infrared reflection-absorption spectroscopy (IRRAS) measurement (Fig. 3C). Furthermore, the high absorbance signal of up to A = 140 mOD extracted from a protein monolayer demonstrates the strong vibrational enhancement of our metasurface design, which exceeds the performance of widely used metal antenna geometries (*22*) by more than one order of magnitude (Fig. S6). Combined with an experimental noise level of 1.8 mOD, this value corresponds to a detection limit of 2130 molecules per μm^2 (Fig. S7).

Miniaturization of IR sensor devices has traditionally been challenging due to the need for scaled down Fourier-transform (FTIR) spectrometers or frequency scanning laser sources (*23*). Recent sensor-on-chip approaches based on thin-film optical waveguides have made progress with monolithic integration, where the light source, sensing element and detector are fabricated on a single chip (*24–26*). In comparison, our technique enables a complementary integration scheme in which the pixelated metasurface sensor can be combined with an IR imaging detector such as a high resolution microbolometer or a mercury cadmium telluride (MCT) focal plane array (Fig. S8). When illuminated with an external broadband light source, this arrangement can overcome the need for a mid-infrared spectrometer in a compact footprint. Furthermore, our scheme addresses several constraints of complete monolithic integration, such as the limited operating range of chip-based light sources and detectors (*27*), as well as sensitivity limitations caused by the low near-field enhancement factors of conventional waveguides (*26*).

We assess the capability of our metasurface sensor for imaging-based spectrometer-less fingerprint detection by calculating the integrated reflectance signal from the spectral data of each metapixel. These integrated signals are analogous to a readout of the metasurface's optical response with a broadband detector before (I_0) and after (I_S) addition of the protein layer (Fig. 3D) and are used to calculate metapixel absorbance signals via $A = -\log(I_S/I_0)$, which are then rescaled between 0 and 100 (Fig. 3E). The resulting barcode-like spatial absorption map of the protein A/G monolayer clearly shows the spectral location and relative intensity distribution of the characteristic amide I and II absorption bands as two distinct high signal regions of the image, providing chemically specific fingerprint detection in a miniaturized design and without the need for spectrometry. This functionality is enabled by the spectrally clean high-Q resonances of the dielectric metapixels and cannot be achieved with metapixels based on conventional metal antennas due to linewidth limitations (Fig. S9). In addition to protein A/G, we also tested a polymer mixture composed of polymethyl methacrylate (PMMA) and polyethylene (PE) as well as glyphosate pesticide to cover applications in fields as diverse as biosensing, materials science and environmental monitoring. In all three cases, the molecular barcodes feature mutually distinct high intensity image regions unique to the vibrational signature of the investigated analytes (Fig. 4A), underscoring the chemical identification capability.

Our barcoding technique offers the potential for identifying molecular species in arbitrary analyte compositions through pattern recognition based on a library of multiple molecular barcode signatures (Fig. S10). To illustrate this approach, we detect a series of predefined mixtures of PMMA and PE polymer molecules deposited on the metasurface using thermal evaporation. Figure 4B shows molecular barcodes for pure PMMA and PE as well as PMMA/PE mixing ratios of 0.25, 0.50, and 0.75. The characteristic molecular signatures of PMMA and PE appear as distinct image features in the top and bottom halves of the barcode matrix, respectively. When increasing the relative amount of PE in the mixture, we observe a substantial increase of the PE signal versus mixing ratio combined with an associated decrease of the PMMA signal.

We carry out further image-based analysis by decomposing the barcode matrices of all mixing states Y_{mix} into a linear combination of the PMMA and PE molecular barcodes via

$$Y_{\mathrm{mix}} = \beta_{\mathrm{PMMA}} \cdot X_{\mathrm{PMMA}} + \beta_{\mathrm{PE}} \cdot X_{\mathrm{PE}}, \quad (1)$$

where X_{PMMA}, X_{PE} are the input barcodes of the pure materials and β_{PMMA}, β_{PE} are the output coefficients associated with the analyte content on the surface (Fig. 4B, center). The PMMA and PE polymer amounts obtained from our image decomposition analysis accurately capture the linear variation of the polymer composition, highlighting the rich chemical and compositional information available from such absorption maps. Although simple linear decomposition is implemented in this demonstration, non-linear processes such as in biomolecular interactions involving multiple analytes and kinetics are foreseen to employ more sophisticated neural network-based image recognition methods and machine learning (*28*, *29*).

Our nanophotonic technique provides the prospects of infrared absorption spectroscopy without the need for complex instrumentation. The Si-based pixelated metasurface is compatible with CMOS technology for low-cost wafer-scale sensor fabrication and can be combined with state-of-the-art surface functionalization techniques for operation in more complex bioassays (*30*). Sensitivity and Q-factor of our metasurface can be further improved by decreasing the resonator orientation angle, only limited by the inhomogeneity of the nanofabrication. Additionally, even stronger near-field enhancement could be achieved by using more sophisticated designs for meta-atoms. The molecular barcodes obtained with our method offer unique possibilities for advanced image analysis, paving the way towards versatile and sensitive miniaturized mid-infrared spectroscopy devices.

References and Notes

1. B. H. Stuart, *Infrared Spectroscopy: Fundamentals and Applications* (John Wiley & Sons, Ltd, 2005).
2. D. Dregely, F. Neubrech, H. Duan, R. Vogelgesang, H. Giessen, *Nat. Commun.* **4**, 2237 (2013).
3. O. Limaj *et al.*, *Nano Lett.* **16**, 1502–1508 (2016).
4. C. Huck *et al.*, *ACS Nano* **8**, 4908–4914 (2014).
5. F. Neubrech, C. Huck, K. Weber, A. Pucci, H. Giessen, *Chem. Rev.* **117**, 5110–5145 (2017).
6. L. Dong *et al.*, *Nano Lett.* **17**, 5768–5774 (2017).
7. B. Cerjan, X. Yang, P. Nordlander, N. J. Halas, *ACS Photonics* **3**, 354–360 (2016).
8. A. I. Kuznetsov, A. E. Miroshnichenko, M. L. Brongersma, Y. S. Kivshar, B. Luk'yanchuk, *Science* **354**, aag2472 (2016).
9. A. Y. Zhu, A. I. Kuznetsov, B. Luk'yanchuk, N. Engheta, P. Genevet, *Nanophotonics* **6**, 1–20 (2017).
10. A. Arbabi, Y. Horie, M. Bagheri, A. Faraon, *Nat. Nanotechnol.* **10**, 937–943 (2015).
11. M. Decker *et al.*, *Adv. Opt. Mater.* **3**, 813–820 (2015).

12. M. Khorasaninejad *et al.*, *Science* **352**, 1190–1194 (2016).
13. D. Lin, P. Fan, E. Hasman, M. L. Brongersma, *Science* **345**, 298–302 (2014).
14. M. Caldarola *et al.*, *Nat. Commun.* **6**, 7915 (2015).
15. M. F. Limonov, M. V. Rybin, A. N. Poddubny, Y. S. Kivshar, *Nat. Photonics* **11**, 543–554 (2017).
16. C. Wu *et al.*, *Nat. Commun.* **5**, 3892 (2014).
17. S. Campione *et al.*, *ACS Photonics* **3**, 2362–2367 (2016).
18. M. Rybin, Y. Kivshar, *Nature* **541**, 164–165 (2017).
19. See supplementary materials.
20. Kai Chen, R. Adato, H. Altug, *ACS Nano*, 7998–8006 (2012).
21. C. Wu *et al.*, *Nat. Mater.* **11**, 69–75 (2011).
22. S. Bagheri *et al.*, *ACS Photonics* **2**, 779–786 (2015).
23. F. K. Tittel, D. Richter, A. Fried, in *Solid-State Mid-Infrared Laser Sources*, I. T. Sorokina, K. L. Vodopyanov, Eds. (Springer Berlin Heidelberg, Berlin, Heidelberg, 2003), pp. 458–529.
24. B. Schwarz *et al.*, *Nat. Commun.* **5**, 4085 (2014).
25. A. Harrer *et al.*, *Sci. Rep.* **6**, 21795 (2016).
26. M. Sieger, B. Mizaikoff, *Anal. Chem.* **88**, 5562–5573 (2016).
27. H. Lin *et al.*, *Nanophotonics* **7**, 393–420 (2017).
28. G. E. Hinton, *Science* **313**, 504–507 (2006).
29. Y. LeCun, Y. Bengio, G. Hinton, *Nature* **521**, 436–444 (2015).
30. S. Jiang *et al.*, *Nanoscale* **5**, 3127 (2013).
31. D. Rodrigo *et al.*, *Science* **349**, 165–168 (2015).
32. X. Gai, D.-Y. Choi, B. Luther-Davies, *Opt. Express* **22**, 9948 (2014).
33. P. Bassan, M. J. Weida, J. Rowlette, P. Gardner, *Analyst* **139**, 3856–3859 (2014).
34. H. P. Erickson, *Biol. Proced. Online* **11**, 32–51 (2009).

Acknowledgments: The authors would like to thank Rui Guo, Eduardo Romero Arvelo and Daniel Rodrigo for useful discussions. We acknowledge École Polytechnique Fédérale de Lausanne and Center of MicroNano Technology for nanofabrication. Sample fabrication was performed in part at the ACT node of the Australian National Fabrication Facility. **Funding:** The research leading to these results has received funding from European Research Council (ERC) under grant agreement no. 682167 VIBRANT-BIO and the European Union Horizon 2020 Framework Programme for Research and Innovation under grant agreements no. 665667 (call 2015), no. 777714 (NOCTURNO project),

no. FETOPEN-737071 (ULTRACHIRAL project), and no. 644956 (RAIS project). The authors acknowledge the support of the Australian Research Council (ARC). **Author contributions:** A.T, D.N.N., Y.S.K, and H.A. conceived and designed the research. A.L., F.Y., and D.-Y.C. fabricated the dielectric metasurfaces. A.T. and A.L. carried out optical measurements and analyzed data. A.L. and M.L. carried out numerical simulations. All authors contributed to writing the manuscript. **Competing interests:** The authors declare no competing interests. **Data and materials availability:** The authors declare that the data supporting the conclusions of this study are available within the article and its supplement. Additional data related to the article are available from the corresponding author upon reasonable request.

Supplementary Materials:

Materials and Methods

Supplementary text

Figures S1-S10

References (*31–34*)

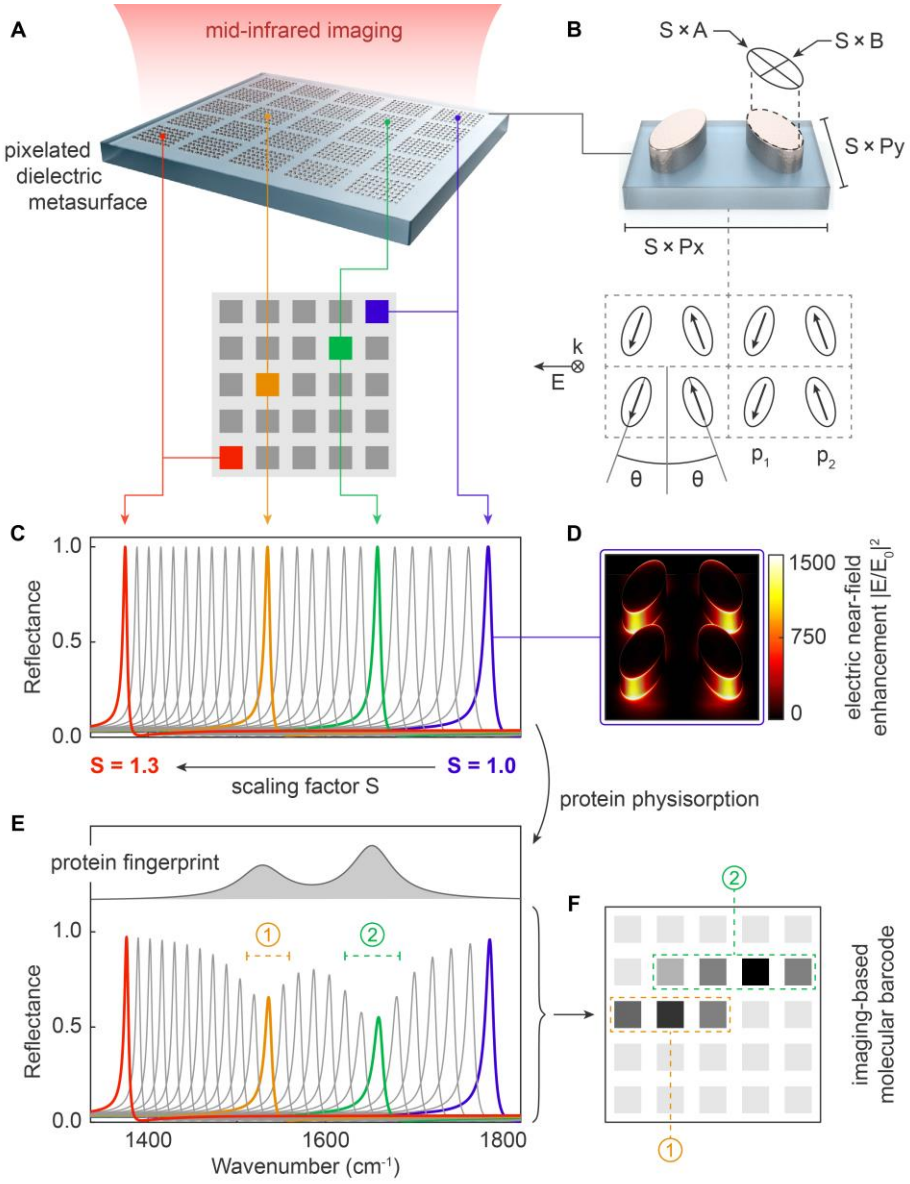

Fig. 1: Molecular fingerprint detection with pixelated dielectric metasurfaces. (**A**) Pixelated metasurface composed of a two-dimensional array of high-Q resonant metapixels with resonance frequencies tuned over a target molecular fingerprint range. (**B**) Spectrally clean high-Q > 200 resonances are provided by zig-zag arrays of anisotropic a-Si:H resonators. Resonance frequencies are controlled by scaling the unit cell lateral dimensions by a factor *S*. (**C**) Numerically simulated metapixel reflectance spectra for different values of the scaling parameter *S*, chosen to cover the amide band spectral region around 1600 cm^{-1}. Geometrical parameters are A = 1.96 µm, B = 0.96 µm, Px = 3.92 µm, and Py = 2.26 µm, with a fixed structure height of H = 0.7 µm and an orientation angle of θ = 20°. (**D**) Simulated electric near-field intensity enhancement $|E/E_0|^2$ for S = 1, where $|E_0|$ denotes the incident field amplitude. (**E**) The envelope of metapixel reflectance amplitudes reproduces the absorption fingerprint of an adjacent model protein layer (top inset). (**F**) Conceptual sketch of a molecule-specific barcode produced by imaging-based readout of the metasurface's reflectance response. Image regions 1 and 2 indicate the spatially-encoded vibrational information from the corresponding metapixel resonances in panel (E).

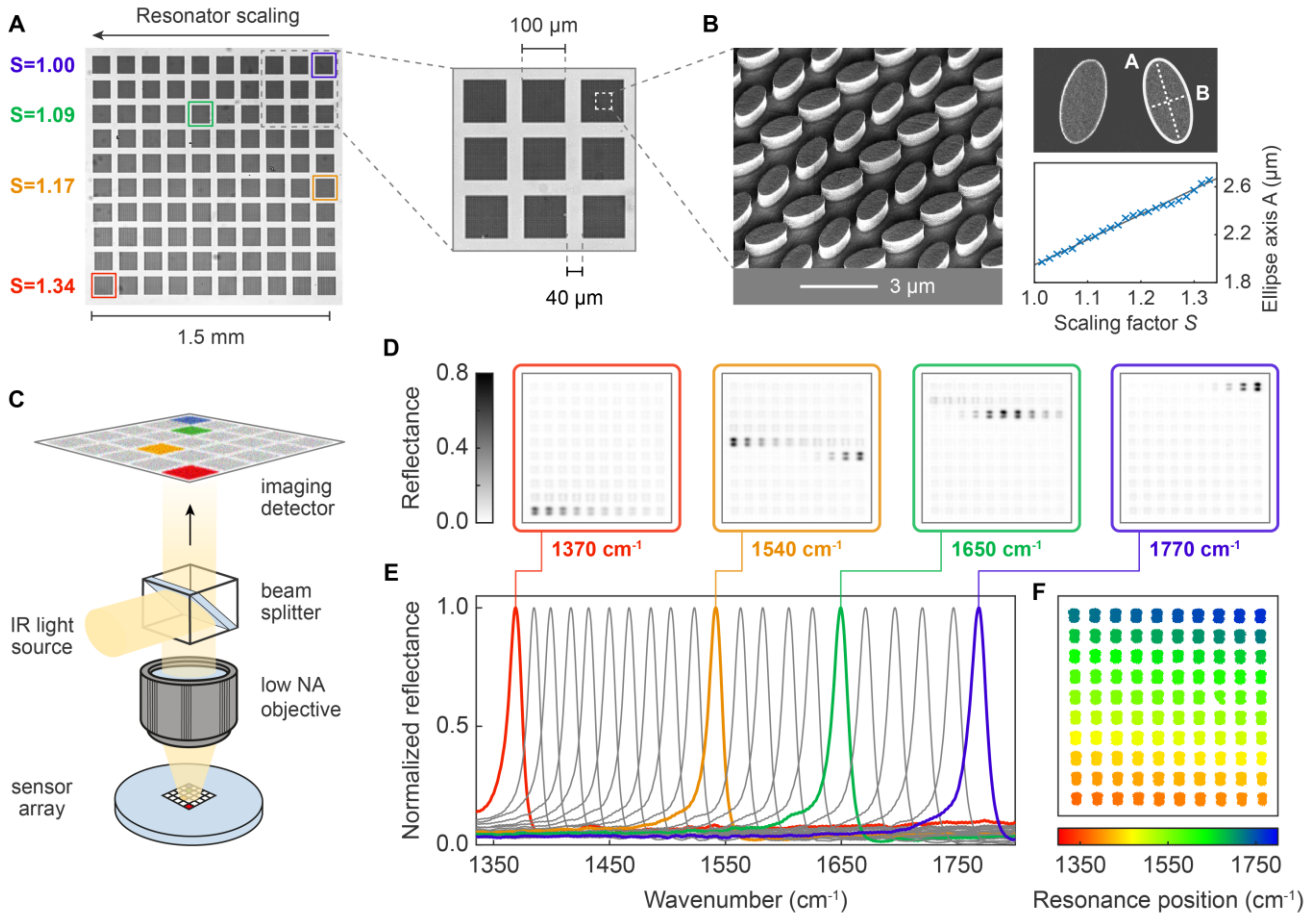

Fig. 2: Experimental realization of the pixelated metasurfaces. (**A**) Optical images of the fabricated 100 pixel metasurface. (**B**) SEM micrographs confirm the linear relationship between scaling factor and ellipse feature size. (**C**) Sketch of the imaging-based mid-IR microscopy system. (**D**) Reflectance images of the pixelated metasurface recorded at four specific wavenumbers in the mid-IR spectral range. (**E**) Normalized reflectance spectra for 21 of the 100 metapixels. Resonance positions of the colored curves correspond to the respective reflectance images in panel (E). (**G**) Extracted resonance positions for all metapixels.

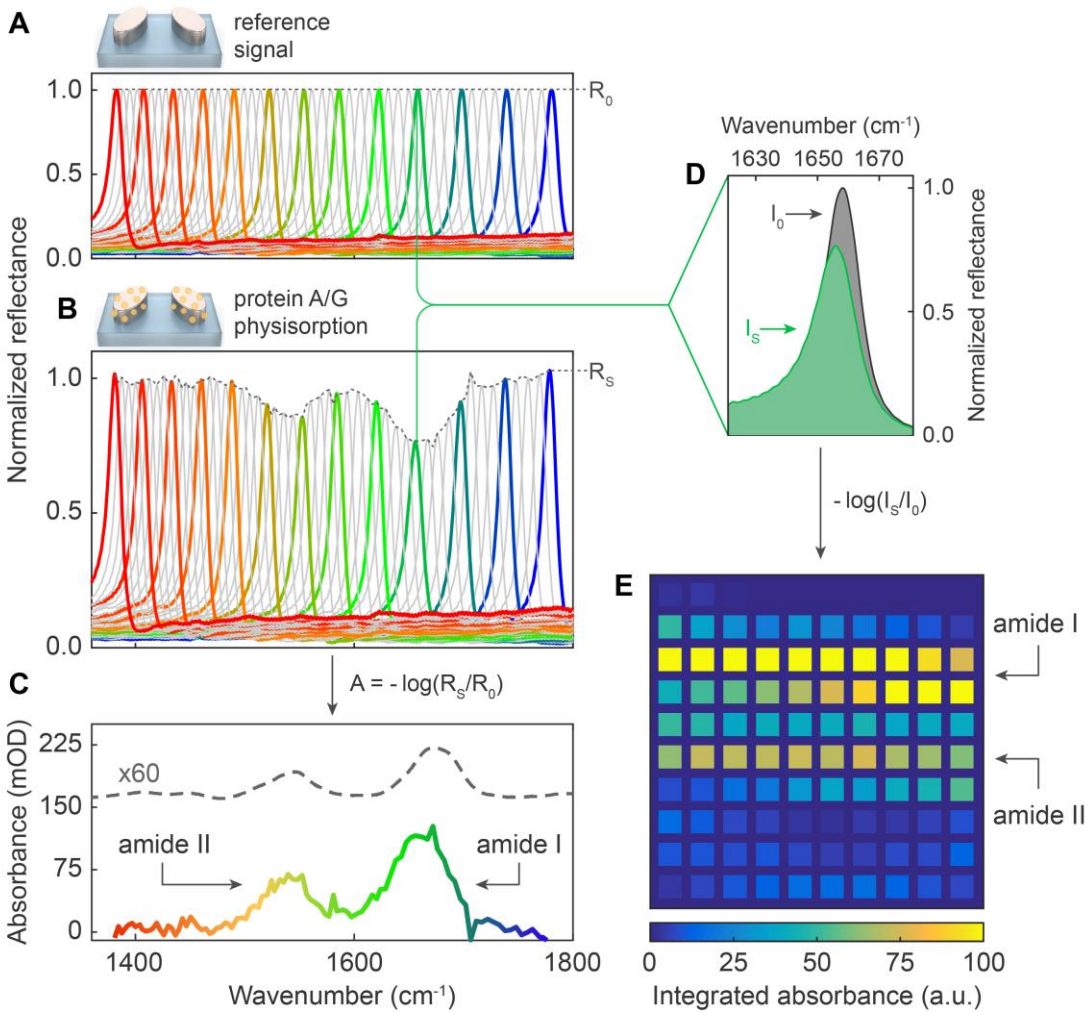

Fig. 3: Molecular fingerprint retrieval and spatial absorption mapping. (**A**) Normalized metapixel reflectance spectra before physisorption of a protein A/G monolayer. R_0 indicates the envelope of peak reflectance amplitudes (dashed line). (**B**) Normalized spectra after protein physisorption, including reflectance envelope R_S (dashed line). (**C**) Protein absorption fingerprint calculated from the reflectance envelopes R_0 and R_S compared to an independent IRRAS measurement (dashed line, scaled and offset for clarity). (**D**) Broadband spectrometer-less operation of the metasurface can be emulated by integrating the reflectance signal of all pixels. (**E**) Spectral integration translates the absorption signature in panel (C) into a 2D spatial absorption map, which represents the molecular barcode of the protein.

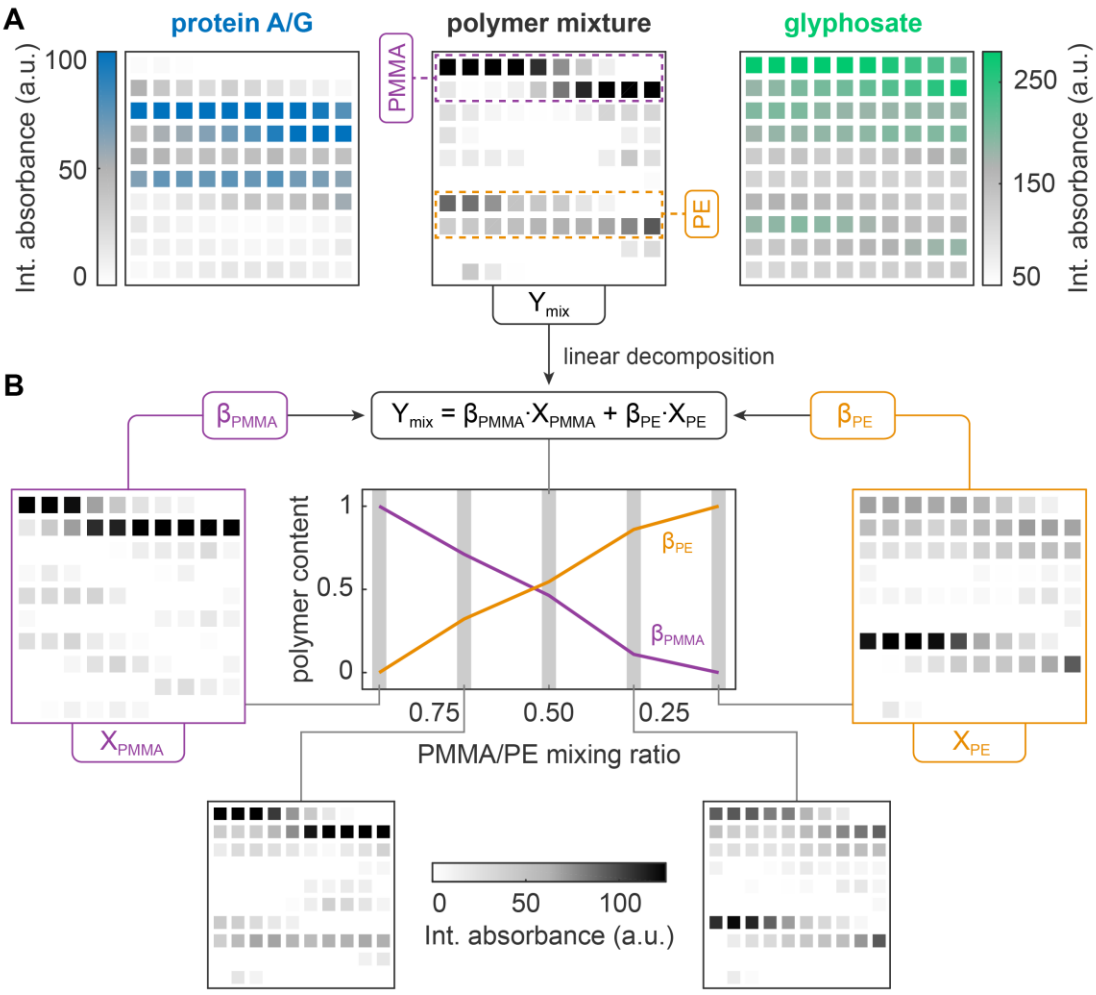

Fig. 4: Imaging-based chemical identification and compositional analysis. (**A**) Molecular barcodes of protein A/G, a mixture of PMMA and PE polymers, and glyphosate pesticide reveal the distinct absorption fingerprints of the analytes. (**B**) Barcode matrices for PMMA/PE polymer mixtures with several mixing ratios. Linear decomposition analysis of all mixing states *Y* with respect to the pure PMMA and PE barcode matrices confirms accurate readout of the deposited polymer ratios.

Supplementary Materials for

Imaging-based molecular barcoding with pixelated dielectric metasurfaces

Andreas Tittl, Aleksandrs Leitis, Mingkai Liu, Filiz Yesilkoy, Duk-Yong Choi, Dragomir N. Neshev, Yuri S. Kivshar, and Hatice Altug*

*Corresponding author. Email: hatice.altug@epfl.ch

This PDF file includes:

Materials and Methods

Numerical calculations

Simulations of the metasurface's optical response were performed using the frequency domain finite element (FEM) Maxwell solver contained in CST STUDIO SUITE 2017 and the unit cell geometry was approximated using a tetrahedral mesh. Base values of the resonator geometrical parameters were defined as Px = 3.92 µm, Py = 2.26 µm for the unit cell periodicities, and A = 1.96 µm, B = 0.96 µm for the ellipse long and short axes, with an orientation angle of $\theta = 20°$. The height of the resonators was fixed at H = 0.7 µm. To vary the resonance frequency of the resonators, all unit cell dimensions except resonator height were scaled with a factor S, linearly interpolated between 1.00 and 1.30 in 25 steps. Refractive index values for the hydrogenated amorphous silicon (a-Si:H) resonators were taken from mid-infrared ellipsometry measurements carried out on a 0.7 µm thick a-Si:H film on a MgF_2 substrate, yielding average values of n = 3.21 and k = 0.00 in the target spectral range. The refractive index of MgF_2 was taken as n = 1.31. To demonstrate protein detection, the chip surface was covered with a 2.5 nm thick conformal model protein layer. The refractive index of this layer was described using a 2-Lorentzian protein permittivity model with parameter values taken from (*31*).

Pixelated metasurface fabrication

All sample fabrication was carried out on magnesium fluoride (MgF_2) chips, which were chosen due to their low absorption and low refractive index in the mid-IR spectral range. A hydrogenated amorphous silicon (a-Si:H) layer of 0.7 µm thickness was deposited onto the chips by plasma-enhanced chemical vapour deposition as described previously (3*2*), followed by the spin coating of a double layer of polymethyl methacrylate (PMMA) resist of different molecular weights (495K and 950K). The elliptical resonator pattern was defined by 100 keV electron beam lithography. An Al_2O_3 hard mask (40nm thickness) was produced via evaporation and wet-chemical lift-off and the ellipse pattern was subsequently transferred into the underlying a-Si:H layer by fluorine-based dry plasma etching. Finally, the Al_2O_3 hard mask was removed by 2 min of RCA 1 wet etching (water, ammonium hydroxide and hydrogen peroxide in ratio 5:1:1) at 80°C.

Imaging-based metasurface measurements

The optical response of our metasurface chips was characterized with a Spero laser-based spectral imaging microscope (Daylight Solutions Inc., San Diego, CA, USA). The microscope is equipped with four quantum cascade laser heads, which allow continuous spectral tuning from 946 cm^{-1} to 1800 cm^{-1}. For imaging, a low magnification objective (4X, 0.15 NA) was used, which covers a 2 x 2 mm^2 field of view (FOV) and delivers 24 µm diffraction limited spatial resolution at 1655 cm^{-1}. For a full description of the Spero microscopy system see Ref. (*33*). All optical measurements of the metapixel array were carried out in reflection mode and normalized to the reflection signal of a plain gold mirror. Measurements were performed in the spectral

range from 1300 cm^{-1} to 1800 cm^{-1} with 0.5 cm^{-1} spectral resolution. To address backscattering effects from the MgF_2 substrate, a background measurement was taken on an empty area of the chip, spatially filtered to remove surface impurities, and subtracted from the metapixel array data. A low pass filter was applied to decrease interference effects from the laser system. During each measurement, 480 x 480 pixel reflectance images were captured for each laser frequency point in the target spectral range. To obtain reflectance spectra for individual metapixels, we first located the image pixels corresponding to the area of an individual metapixel. Subsequently, the spectrally resolved reflectance data from these image pixels was averaged to yield the full metapixel spectrum. To obtain the integrated absorbance signals displayed in the molecular barcode matrices, we performed trapezoidal numerical integration of the reflectance spectra over the range from 1300 cm^{-1} to 1800 cm^{-1}. The influence of side band reflection signals was reduced by applying a Gaussian band pass filter centered on the resonance position. On average, dust or other analyte impurities produced absorbance signal outliers for approximately 1 of 100 pixels per measurement. Affected pixels were excluded from the absorption maps. Due to the high number of metasurface pixels, a moving mean filter with a filter width of 4 was applied to improve the clarity of the absorption maps. For presentation, the protein A/G signal was rescaled by normalizing between 0 and 100 after applying a threshold for the maximum signal. The maps of the following analytes where scaled with respect to the protein A/G map.

Analyte preparation

For the chemical identification measurements, protein A/G was diluted in 10 mM acetate solution at 0.5 mg/mL concentration. The sensor chip was incubated with protein A/G solution to allow protein physisorption, followed by rinsing with deionized water to remove unbound protein and agglomerates. Glyphosate pesticide was diluted in deionized water at 5 mg/ml concentration and spin coated on the sample at 6000 rpm spin speed. Polymethyl methacrylate with an average molecular weight of 350,000 and medium density polyethylene were deposited by thermal evaporation. The deposition rate and layer thickness were measured with a quartz crystal oscillator. Layer thicknesses for pure PMMA and PE before mixing were 10 nm and 40 nm, respectively.

Infrared reflection absorption spectroscopy

A reference measurement for the protein A/G absorption spectrum was acquired using infrared reflection absorption spectroscopy. A protein A/G monolayer was physisorbed on a gold mirror using the procedure described in the “Analyte preparation” section above. The spectrum of the analyte was measured with a Fourier transform infrared spectrometer (Bruker Vertex 80V) using a variable angle reflection accessory (Harrick SEAGULL). The measurements were made at 75 degree light incidence angle with p polarized light.

Supplementary Text

1. Theoretical analysis of the high-Q metapixel design based on zig-zag arrays

The high-Q metasurface design utilized in this work is based on zig-zag arrays of elliptical dielectric meta-atoms, where the collective resonance is formed by the electric dipole modes polarized along the long axis of each individual meta-atom. For a lossless system, the linewidth of the resonance depends on the scattering loss, which is determined by the overlapping of the mode profile and the field polarization of the scattering channels. For the periodic zig-zag metasurface studied here, the scattering channels are the zeroth order plane waves propagating in the normal direction; the overlapping of the mode profile and the plane wave is determined by the net-electric dipole moment in each unit cell.

The zig-zag design allows us to precisely control this overlap by fine-tuning the unit cell geometry including the orientation angle θ of the meta-atoms. When the collective mode is excited, the dominant component of the dipole moments of the meta-atoms (p_{y}) are actually perpendicular to the incident field polarization E_x^i as shown in Fig. S1A. However, due to the antisymmetric distribution of the components ($p_{1,\mathrm{y}} = -p_{2,\mathrm{y}}$), the out-coupling with the plane wave of E_y polarization is forbidden, and thus the overall scattering loss of the collective mode is suppressed significantly. In fact, only the p_{x} component is nonzero ($p_{1,\mathrm{x}} = p_{2,\mathrm{x}}$) and therefore contributes to the scattering loss.

For simplicity, we assume that the zig-zag array is lossless and positioned in a homogenous background. The forward and backward scattered fields are contributed by the collective dipole resonance with nonzero net dipole moment p_x, which can be expressed as

$$E^f = E_x^i + \frac{i\omega\eta}{2A} p_x, \tag{1a}$$

$$E^b = \frac{i\omega\eta}{2A} p_x, \tag{1b}$$

where η is the wave impedance of the surroundings and A is the area of the unit cell. The net dipole moment within a unit cell can be further expressed as

$$p_x = i2Iu \sin\theta/\omega, \tag{2}$$

where u is the normalized dipole moment of a single meta-atom. I is the corresponding frequency-dependent current amplitude that captures the resonant behavior, which can be calculated via

$$I = \frac{E_x^i u \sin\theta}{Z}, \tag{3}$$

with Z being the effective impedance of the meta-atom under the collective resonance, taking into account all the mutual interaction. Generally, the effective impedance around a single resonance can be approximated with an RLC circuit:

$$Z = -i\omega L - \frac{1}{i\omega C} + R, \tag{4}$$

where R is the effective resistance and is contributed solely by the radiative loss in a lossless system. From energy conservation, it requires that

$$\left|E_x^i\right|^2 = \left|E^f\right|^2 + \left|E^b\right|^2. \tag{5}$$

Substituting Eqs. (1a) to (4) into Eq. (5), and using the identity: $\mathrm{Re}(1/Z) = \mathrm{Re}(Z^*)/|Z|^2 = R/|Z|^2$, we obtain the following relation between the effective resistance R and the orientation angle θ:

$$R = \frac{2\eta u^2 \sin^2\theta}{A}. \quad (6)$$

Since the quality factor $Q = R^{-1}\sqrt{L/C}$ and the effective inductance L and capacitance C do not change significantly when θ is small, it is expected that the quality factor $Q \propto 1/\sin^2\theta$, which grows dramatically as the orientation angle θ decreases.

To confirm the effect, we simulate the resonance behavior using the geometrical parameters from Fig. 1 of the main text with a scale factor S = 1.0; by changing the orientation angle while keeping other parameters unchanged, we clearly observe the asymptotic behavior of the quality factor as θ decreases (Fig. S1B). Although in practice, the Q-factor achievable is limited by various factors including material loss and finite sample size, our zig-zag concept provides a straightforward way to control the Q-factor and can be easily applied to meta-atom designs other than ellipses.

In general, the higher Q-factors associated with lower orientation angles increase the sensitivity of the resonators to changes in the environment, leading to improved fingerprint detection performance. On the other hand, this increased sensitivity also makes the system more susceptible to small variations in structure size associated with nanofabrication inhomogeneity. In experiments, an orientation angle of $\theta = 20°$ was chosen to provide a trade-off between these two factors by delivering experimental
Q-factors above 100 within our fabrication tolerances.

Unlike many geometries based on leaky guiding modes where the electric field is mostly confined within the high-index material, this particle-based collective dipole resonance allows strong near-field enhancement at the surface of the meta-atom, which is a desirable feature for surface-based molecular sensing. Figure S1C shows the enhancement of the electric near-field intensity on two different cut-planes: one is a horizontal cut-plane 2.5 nm away from the substrate, the other is a vertical cut-plane across the long-axis of the meta-atom. We find strongly enhanced electric near-fields in between the meta-atoms, with electric near-field intensity enhancement values of up to 1500. This enhancement value is which is within the 10^3-10^4 enhancement range of many widely studied metal-based antenna geometries for use in practical applications (*5*). In general, high field confinement is easier to achieve in metallic resonators due to the strong contrast between the dielectric functions of the metal and the non-metallic environment. However, this field localization comes at the expense of the resonance Q-factor due to the intrinsic damping of the metal. Even though higher field enhancements values of 10^7 can be achieved using metallic nanogap antennas with inter-element spacings below 10 nm (*6*), they are difficult to fabricate with the reliability and reproducibility needed for practical sensing devices.

Figure S1D again highlights the near-field intensity on the meta-atom surface, where we plot the amplitude distribution along the three line-cuts shown in Figure S1C. Note that z = 0 nm and z = 700 nm represent the surface of the substrate and the top surface of the meta-atoms, respectively; we choose z = 2.5 nm and z = 702.5 nm to match the thickness of the molecule layer.

Significantly, the enhanced near-fields are localized in distinct hot-spots on the surface of the meta-atoms, which is a characteristic feature of many nanophotonic systems based on localized resonators. During sensing experiments, the target analytes interact with both the low

and high intensity regions of the electric field around the meta-atom. Therefore, the effective enhancement of the molecular absorption signature is determined by the averaged electric near-field intensities around the meta-atom. We estimate this effect by averaging the simulated electric near-field intensities over a 2.5 nm thick layer around the meta-atoms and obtain an effective enhancement factor of 320 for a scaling factor of S=1.0. The reduced effective enhancement compared to the hot-spot values is common to all localized resonance geometries and is similarly found in plasmonic platforms (*4*).

These performance considerations are valid as long as the analyte presented to the surface exhibits sufficient spatial uniformity, which is fulfilled in a multitude of analyte systems of interest such as molecular monolayers, biological species (lipids, proteins, DNA, etc.) suspended in buffer solutions, or layers of solid analytes deposited by, e.g., evaporation. Low numbers of molecules can be resolved as long as a statistical distribution over the meta-atom surface is ensured, or additional surface functionalization is employed to selectively attach the molecules in the hot-spot regions.

2. Pixel size considerations and advanced sampling techniques

One of the central features of our pixelated metasurface approach is the spatial encoding and separation of spectral information. Therefore, the metasurface's performance is determined by the number and size of individual metapixels for a given detector field of view. In general, a single metapixel covering the detector field of view will provide the best performance in terms of signal-to-noise ratio since the analyte absorption signature is amplified and detected over the full area, but will provide spectral information only for a single frequency point. For higher numbers of metapixels p, the spectral resolution increases, but only a reduced fraction of the metasurface area (in general $1/p$) will provide resonant enhancement. In experiments, metapixel sizes of 100 µm x 100 µm were chosen to provide a trade-off between a sufficiently high signal-to-noise ratios and the number of pixels required for 4 cm^{-1} spectral resolution.

Due to the flexibility of our metasurface design, a variety of advanced sampling techniques can be applied to further tailor signal-to-noise ratio and spectral coverage. To illustrate two such concepts, we consider an artificial molecular fingerprint with two features (absorption bands I and II), which exhibit large spectral separation and strongly dissimilar absorption magnitudes (Fig. S2).

First, the retrieval of absorption signatures from weak molecular vibrations can be improved by utilizing metapixels with increased sizes for these frequency points, which results in higher signal-to-noise ratios as outlined above. Likewise, metapixel size can be decreased for spectral regions of strong molecular absorption, maximizing the total number of metapixels in the detector field of view.

Second, the spectral resolution of the absorption bands of interest can be increased by implementing non-uniform frequency sampling. With this approach, denser frequency sampling is employed in spectral regions with fine fingerprint features, whereas the molecular signature is sampled more broadly otherwise (Fig. S2). This technique allows to increase the spectral fidelity of the fingerprint reproduction while keeping the total number of metapixels constant.

3. Scanning electron microscopy characterization of the metasurface

The fabricated pixelated metasurface was extensively characterized using scanning electron microscopy (SEM). Figure S3A shows exemplary SEM images for metapixels with the highest (S = 1.36) and lowest (S = 1.00) scaling factor values defined in the metasurface, confirming the exact reproduction of the target ellipse shape. To provide a thorough analysis of the resonator geometry over the full metasurface area, we extract the unit cell geometrical parameters (ellipse axes lengths and periodicities) from SEM images of 25 metapixels distributed throughout the scaling factor range (Fig. S3B). We find a nearly linear relationship between scaling factor and the geometrical parameters over the full scaling range, which confirms the accuracy and uniformity of our nanostructuring process.

4. Additional spectral characterization of the metasurface

Normalized reflectance spectra for all 100 pixels of the dielectric metasurface are shown in Fig. S4A. We perform full spectral characterization of the metasurface by extracting the resonance positions, linewidths, quality factors and maximum signal amplitudes from the spectral data using a standard peak fitting approach in MATLAB. Spectral properties are presented as a function of pixel number, where #1 corresponds to a scaling factor of S = 1.0 and #100 to S = 1.34, respectively.

We find resonance positions with continuous variation over a spectral coverage range from 1370 cm^{-1} to 1770 cm^{-1} combined with an average linewidth (full width at half maximum, FWHM) of 13.7 cm^{-1} (Fig. S4B,C). This results in an average Q-factor (resonance position / FWHM) of 115 (Fig. 4D). Maximum peak reflectance values are shown in Fig. S4E. The decrease in reflectance for higher pixel numbers (i.e., higher scaling factors) is attributed to the relative decrease of resonator mode volume caused by the fixed resonator height H = 0.7 µm.

5. Extension of metasurface working range

Our dielectric resonator design allows for the straightforward extension of the operating spectral range by increasing the range of scaling factors S. Figure S5A shows simulated reflectance spectra for scaling factors between S = 0.56 and S = 2.0, linearly interpolated in 21 steps. The geometrical parameters before scaling are identical to the design described in the manuscript with Px = 3.92 µm, Py = 2.26 µm for the unit cell periodicities, and A = 1.96 µm, B = 0.96 µm for the ellipse long and short axes, and an orientation angle of $\theta = 20°$.

We find high Q-factor resonances covering the mid-IR molecular absorption band region from 2.5 µm to 10 µm together with a linear relationship between scaling factor and resonance position (Fig. S5B), which facilitates the design of suitable metapixels for arbitrary target absorption bands. The decrease in performance at a wavelength of around 5 µm is due to the intrinsic absorption of a-Si:H in this range, and can be overcome by moving to a different resonator material such as germanium. With the exception of the a-Si:H absorption region, high resonance sharpness (Q > 100) is maintained over the full target wavelength range (Fig. S5C), and Q-factors above 600 can be achieved in the long wavelength region around 10 µm.

6. Performance comparison with traditional metal-based SEIRA geometries

We assess the performance of our dielectric metapixel design by numerically comparing it to a widely used traditional SEIRA approach based on metallic nanostructures. Specifically, we follow the guidelines for periodicity optimized gold nanoantenna SEIRA substrates outlined in Ref. (*22*) to obtain resonant metallic metapixel designs in our target spectral range. The reflectance spectrum of an exemplary gold metapixel displays a pronounced peak centered at 1560 cm^{-1} and a FWHM of 565 cm^{-1} (Fig S6A). The antenna geometry is defined as antenna length 2.1 µm, antenna width 0.14 µm, and antenna height 0.1 µm. The distance between antennas is 1 µm in x-direction and 2 µm in y-direction. Even though gold nanoantennas are used for the following numerical comparison in accordance with Ref. (*22*), comparable performance is obtained for other metals such as silver and copper in the infrared (Fig. S6A).

To gauge the molecular fingerprint detection performance, the metallic metapixel surface is covered with a 2.5 nm thick conformal model protein layer analogous to the simulations for the dielectric metapixels presented in Fig. 1E of the main text. Even though the addition of the protein layer produces a clear change of the resonance lineshape (R_S) compared to the reference spectrum (R_0), the protein-induced reflectance modulation is much lower compared to the dielectric metapixel case (Fig. S6B).

To quantify the performance difference between the metallic and dielectric metapixel designs, we calculate the absorbance signal from the reflectance curves R_0 and R_S via $A = -\log(R_S/R_0)$. We find maximum absorbance signals of around 275 mOD for the dielectric case compared to around 16 mOD for the metallic case, demonstrating that our dielectric metapixel concept can deliver performance improvements of more than one order of magnitude over such metal-based designs (Fig. S6C).

The key differentiating factor of our imaging-based dielectric metapixel concept is its ability to extract molecular fingerprints information from the integrated reflectance signal, which corresponds to the usage of a broadband light source and detector (see Fig. 3 in the main text). To check whether such performance is possible using the previously discussed metallic metapixels, we tune the length of the gold nanoantennas to produce a series of metallic metapixels with resonance frequencies covering the target fingerprint range (Fig. S9A). More specifically, the antenna length is linearly interpolated from 2.1 µm to 3.1 µm in 21 steps while keeping the other geometrical parameters the same.

A direct comparison between the metallic and dielectric metapixel cases is performed by integrating the reflectance spectra in the range from 1340 to 1840 cm^{-1} before (I_0) and after (I_S) addition of the model protein layer. The integrated absorbance signal for both cases is then obtained via $A = -\log(I_S/I_0)$. We find that the integrated signal from the dielectric metapixels clearly reproduces the protein amide I and II absorption signature (Fig. S9B). In strong contrast, the integrated signal from the metallic metapixels is unable to resolve the protein signature, even though a slight variation of the reflectance envelope R_S is still visible in Fig. S6A. Such comparatively poor performance is due to the broad linewidth of the gold nanoantenna resonances and the associated large integrated reflectance signal. Consequently, small protein-induced modulations of the reflectance signal have only a negligible influence on the total integrated signal, making broadband fingerprint detection with such metallic metapixels challenging at realistic signal-to-noise levels.

7. Experimental noise and limit of detection estimation

We estimate the limit of detection of our sensor metasurface by considering the absorbance value of 140 mOD obtained from a protein monolayer (see Fig. 3C in the manuscript) together with the noise level of our experiments. The experimental noise level (which is determined by factors such as detector noise, source stability, and optical alignment) can be estimated by capturing a total of $n = 5$ reference metasurface measurements without the presence of any analytes. For all data sets, the envelopes of the peak reflectance values R_i $(i = 1, \cdots, n)$ are derived as shown in the manuscript and the average value of these envelopes is calculated via $R_{\text{avg}} = (R_1 + \cdots + R_n)/n$.

This allows us to determine the absorbance variation

$$\Delta A_i = -\log\left(R_i / R_{\text{avg}}\right) \qquad (7)$$

for each measurement as shown in Fig. S7. Each absorbance variation curve consists of $p = 100$ points consistent with the 100 pixels of the metasurface design, where $\Delta A_i^{(k)}$ denotes the curve value at a specific pixel position with $k = 1, \cdots, p$. The total noise level can be quantified by calculating and averaging the root mean square (RMS) value for all curves, which results in an experimental noise level value of

$$A_{\text{rms}} = \frac{1}{n}\sum_{i=1}^{n}\sqrt{\frac{1}{p}\sum_{k=1}^{p}\left(\Delta A_i^{(k)}\right)^2} = 1.8 \text{ mOD}. \qquad (8)$$

In general, sensors are assumed to reliable detect signals exceeding three times the noise, which is often referred to as the 3σ noise level. In our experiments, we observed an absorbance signal of around $A_{\text{exp}} = 140$ mOD for a protein A/G monolayer, which corresponds to 55220 molecules per μm^2 when assuming densely-packed spherical protein A/G molecules with a diameter of 4.8 nm calculated from their molecular mass (*34*). A comparison of the signal and noise levels results in a detection limit of 2130 molecules per μm^2 for protein A/G detection, assuming a linear relationship between molecular coverage and sensor signal.

Signal-to-noise ratio considerations also play an important role for the broadband operation of our metasurface-based approach, specifically when moving from illumination with a tunable but narrow-band quantum-cascade laser (QCL) to an intrinsically broadband globar source. In general, this transition is associated with a decrease of the available light intensity. However, due to the narrow-band nature of QCLs, the acquisition of the sensor metasurface response in a specific frequency range requires a large number of sequential measurements determined by the desired frequency resolution. For instance, covering the wavenumber range from 1300 cm^{-1} to 1800 cm^{-1} with 4 cm^{-1} resolution requires 125 sequential measurements. In broadband operation, only one single measurement is needed to capture the same information. This advantage enables an increase of the acquisition time by the same factor of 125, greatly improving the signal-to-noise ratio and compensating, in part, the decrease in the intensity of the incident light.

As detailed in Supplementary Section 2, advanced sampling techniques such as tailored pixel sizes and non-uniform sampling can be employed to further improve the signal-to-noise ratio. If additional gains are needed for a target application, high sensitivity pixelated detectors such as mercury cadmium telluride focal-plane arrays can be utilized in place microbolometer arrays.

8. Integration of sensor metasurface and imaging chip

Our molecular fingerprint detection concept allows for a direct integration between sensor and imaging detector by placing the pixelated dielectric metasurface directly on a pixelated broadband IR detector such as a microbolometer or an array based on mercury cadmium telluride (MCT) elements (Fig. S8A). Such an integrated configuration requires the operation of the dielectric metasurface in transmission. In this case, the integrated absorbance from individual metapixels needs to be calculated via $A = -\log[(I_S - I_B) / (I_0 - I_B)]$, where I_0 and I_S denote the broadband readouts of the sensor metasurface before and after the addition of the analyte molecules, and I_B represents the resonance-free background.

We perform molecular detection simulations similar to the ones in Fig. 1 of the manuscript with a design optimized for operation in transmission. This optimization yields geometrical parameters of Px = 3.51 µm, Py = 2.03 µm for the unit cell periodicities, and A = 1.76 µm, B = 1.29 µm for the ellipse long and short axes, with an orientation angle of $\theta = 20°$. Simulated transmittance spectra for scaling factors between S = 1.00 and S = 1.36 (linearly interpolated in 25 steps) are shown in Fig. S8B. Importantly, we find that the envelope of metapixel transmittance spectra still unambiguously reproduces the target molecular absorption fingerprint, with signal modulations up to 30%.

9. Sensor operation with mixtures containing multiple analytes

In Figure 4 of the manuscript, we demonstrated the compositional sensitivity of our sensor platform by investigating a binary mixture of PMMA and PE polymers with different mixing ratios. Subsequently, we introduced a straightforward linear decomposition approach to retrieve the individual amounts of PMMA and PE in the mixture.

It is important to note that the proposed technique is not limited to binary mixtures, but can easily be extended to analyze mixtures containing multiple classes of molecular species. To illustrate this capability, we consider a mixture of four model analytes with corresponding molecular barcodes (Fig. S10). The molecular barcode of this mixture is obtained by combining the barcodes of the individual analytes A-D with predefined mixing ratios and adding a random noise component consistent with the experimentally determined RMS value from Supplementary Section 7. By considering a large number of such barcodes with randomly generated noise components, the error of the subsequent linear decomposition analysis can be estimated via statistical analysis.

Even though the molecular fingerprint of the mixture no longer displays the clear signatures of the constituent analytes, linear decomposition analysis is again able to retrieve the correct relative analyte amounts with high signal-to-noise ratios (Fig. S10). Error bars are determined by calculating the standard deviation of multiple linear decomposition runs with different noise components. Going beyond this example, the number of analytes in the mixture can easily be increased further, provided that the molecular barcodes of the analyte library show sufficient mutual linear independence.

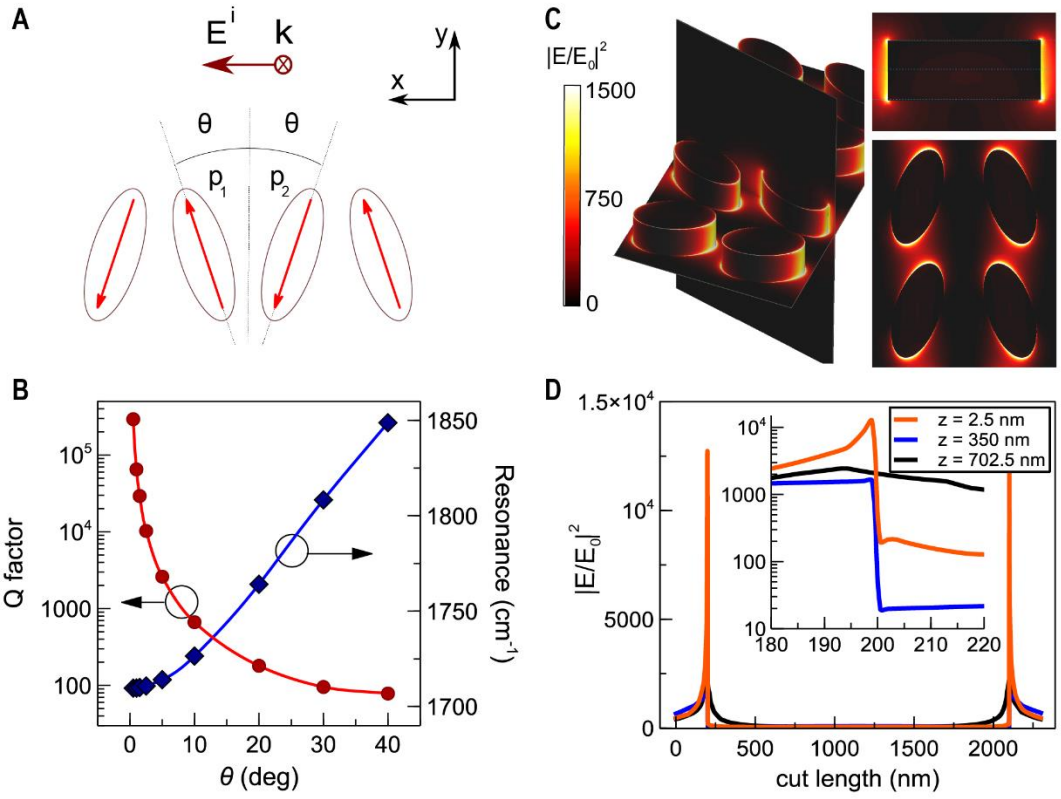

Fig. S1.

Theoretical analysis of high-Q collective resonance based on zig-zag arrays. (A) Schematic of the collective dipole mode of the array when excited with E_x^i polarization. (B) Simulated Q-factors and resonance wavenumbers under different orientation angle θ. The geometries are the same as the one simulated in Fig.1C for S=1.0, except for the changing orientation angle. (C) Simulated electric near-field intensity enhancement $|E/E_0|^2$ at the resonance frequency with orientation angle
$\theta = 20°$, where $|E_0|$ denotes the incident field amplitude. (D) Near-field intensity enhancement $|E/E_0|^2$ along three line cuts, shown as dashed-lines in panel (C). Inset magnifies the part around the boundary between the silicon meta-atom and the surroundings.

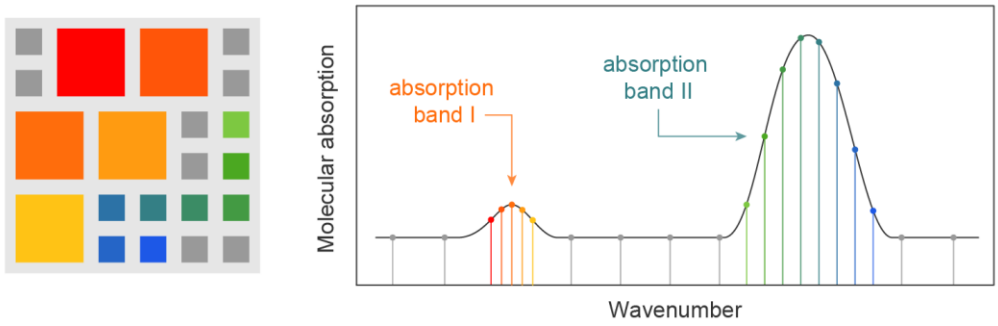

Fig. S2

Advanced sampling techniques. Challenging molecular absorption signatures with large spectral separation and strongly dissimilar absorption magnitudes can be resolved by employing metapixels with tailored sizes as well as non-uniform frequency sampling.

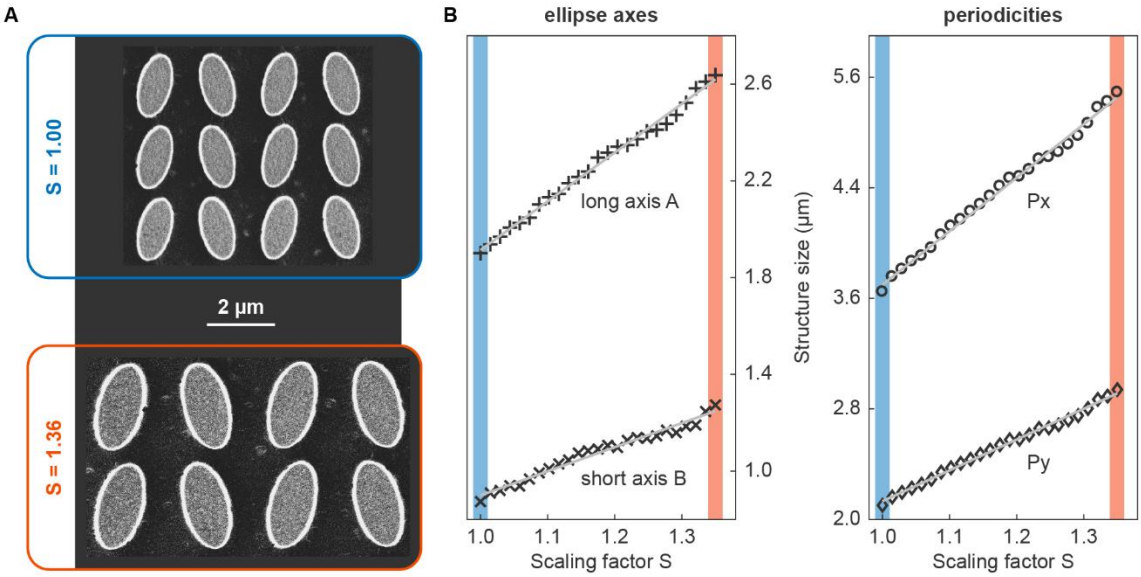

Fig. S3

Scanning electron microscopy analysis. (A) Exemplary SEM images of fabricated metapixels with scaling factors of S = 1.00 and S = 1.36. (B) Extracted geometrical parameters of the resonators for 25 of the 100 metapixels. Grey lines represent the linear trends of the data.

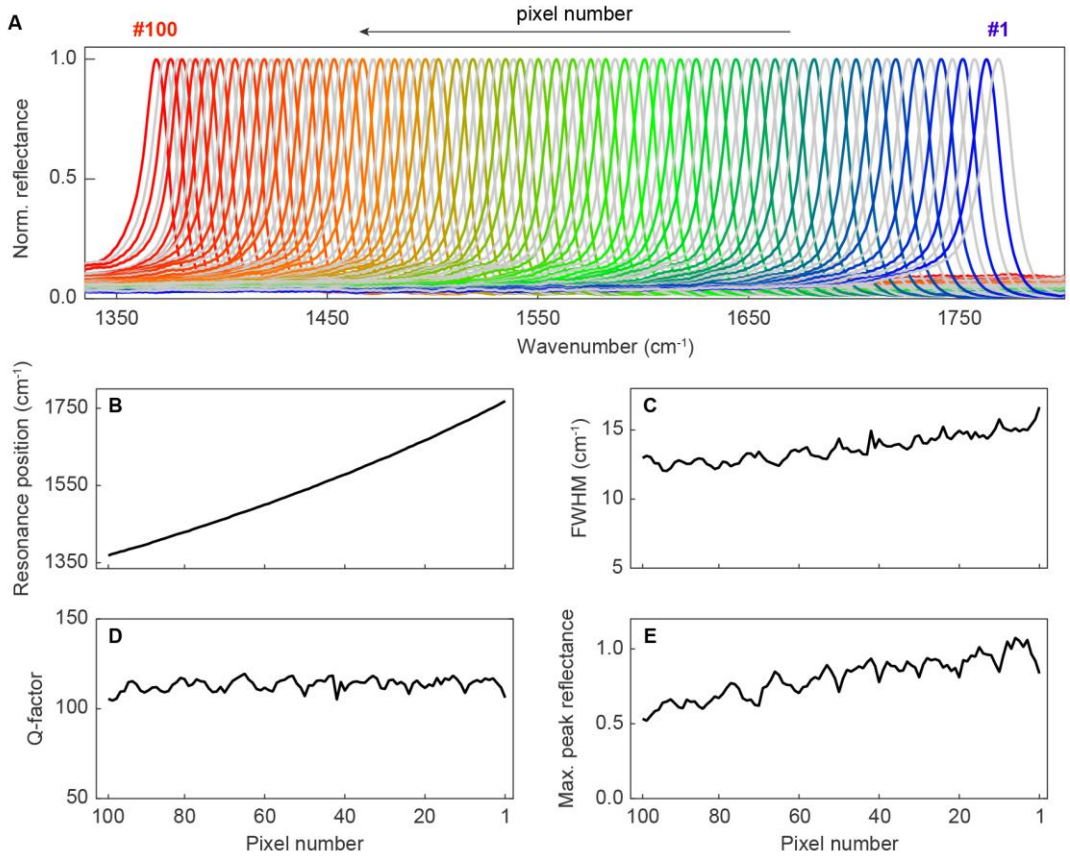

Fig. S4

Spectral characterization of the pixelated dielectric metasurface. (A) Normalized reflectance spectra. (B) Resonance position. (C) Full width at half maximum (FWHM). (D) Resonance Q-factor. (E) Maximum peak reflectance.

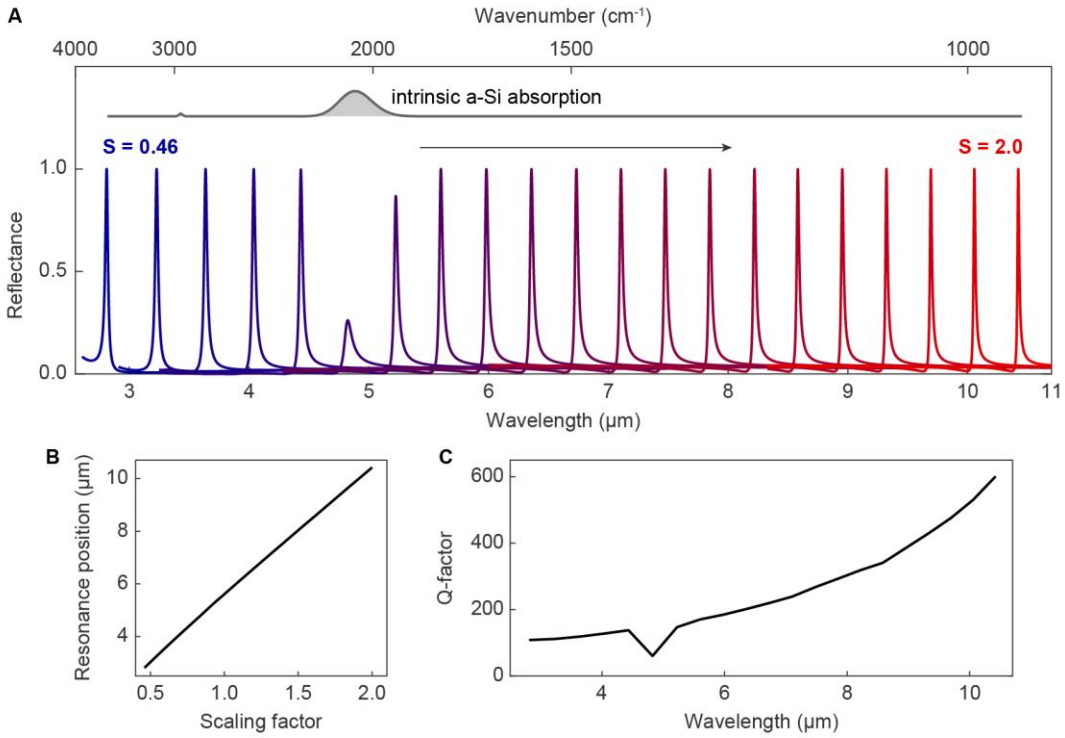

Fig. S5

Extended metasurface design working range. (A) Simulated reflectance spectra for scaling factors ranging from S = 0.56 to S = 2.0. For each spectrum, only the dominant reflectance peak is shown. (B) Resonance position varies linearly with scaling factor over a wide range. (C) Q-factors remain above 100 over the entire wavelength range, with peak values above 600 in the long wavelength region around 10 μm.

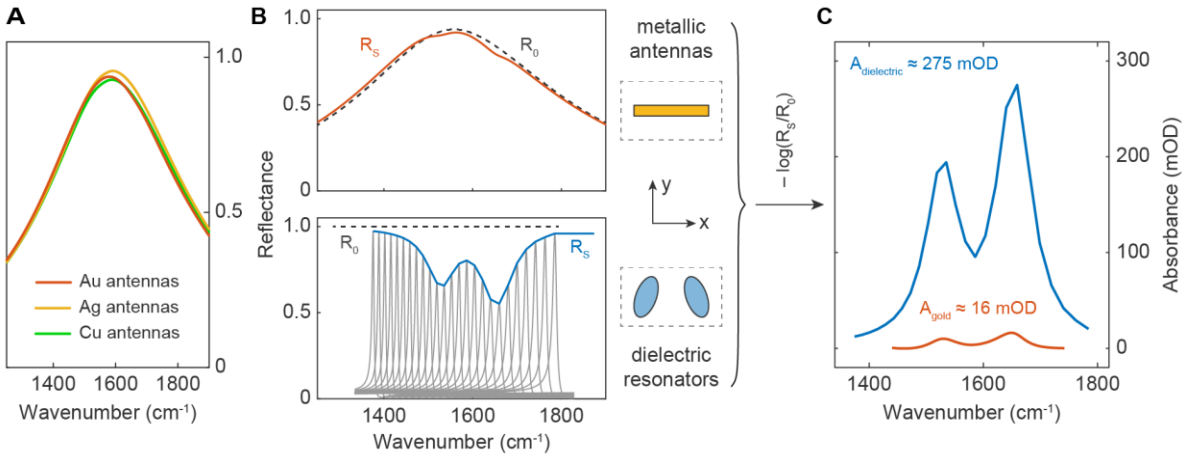

Fig. S6

Molecular fingerprint detection performance comparison. (A) Simulated reflectance spectra for metallic antennas with three different materials. (B) Comparison of simulated reflectance spectra for gold nanoantennas and our dielectric resonators before (R_0) and after (R_S) addition of a conformal model protein layer. (C) Absorbance signal calculated from the reflectance curves R_0 and R_S from panel (A). The dielectric metapixel design provides an absorption signal improvement of over one order of magnitude.

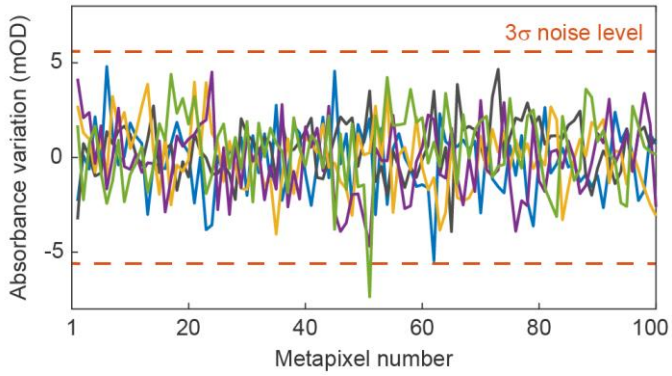

Fig. S7

Experimental noise level. Absorbance variation curves derived from 5 metasurface measurements without the presence of any analytes. We obtain a root mean square noise value of $A_{\mathrm{rms}} = 1.8$ mOD and a corresponding 3σ noise level of 5.4 mOD.

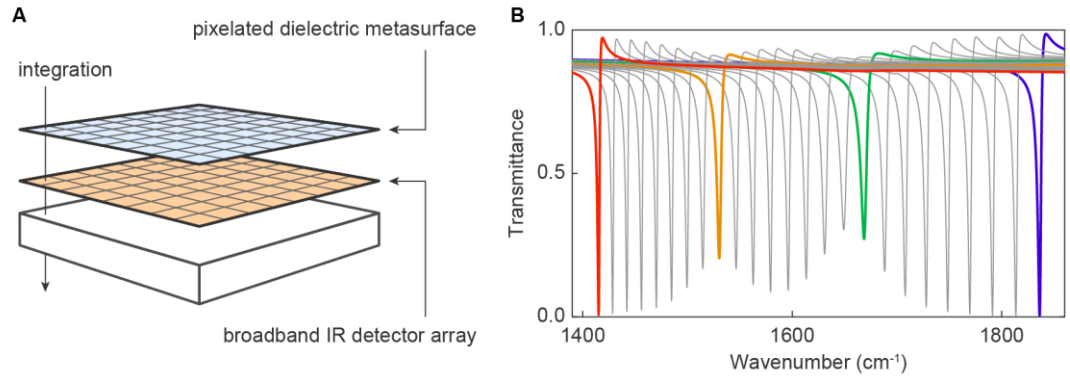

Fig. S8

Towards miniaturized sensor devices. (A) Sketch of a possible configuration for compact imaging-based molecular fingerprint detection. The pixelated metasurface sensor is placed directly on top of a broadband IR detector array. (B) Fingerprint detection performance of the metasurface design in transmission.

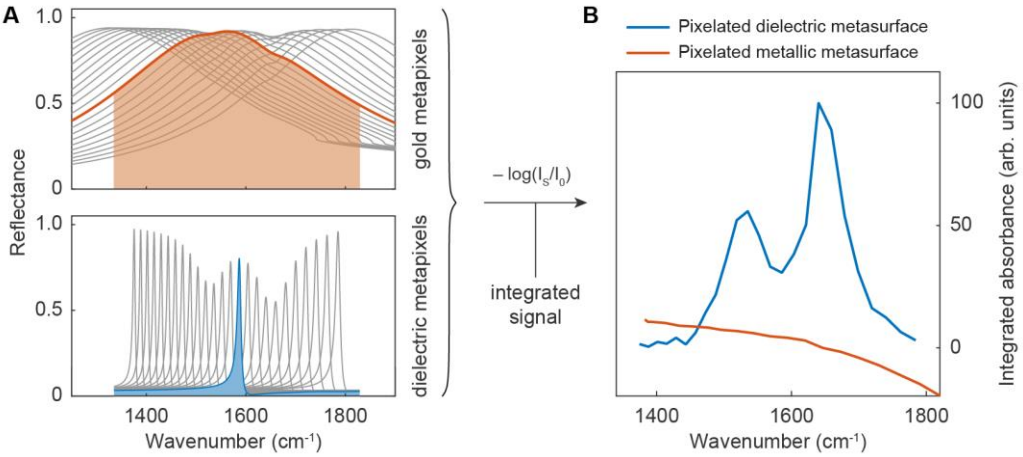

Fig. S9

Performance comparison of imaging-based detection via integrated signals (A) Simulated reflectance spectra for gold and dielectric metapixels designed to exhibit resonances covering the amide I and II spectral range. (B) Integrated absorbance signal obtained by integrating the reflectance data in panel (A) from 1340 to 1840 cm^{-1}. A pixelated metallic metasurface is unable to resolve the amide I and II absorption signature due to the high associated resonance linewidths.

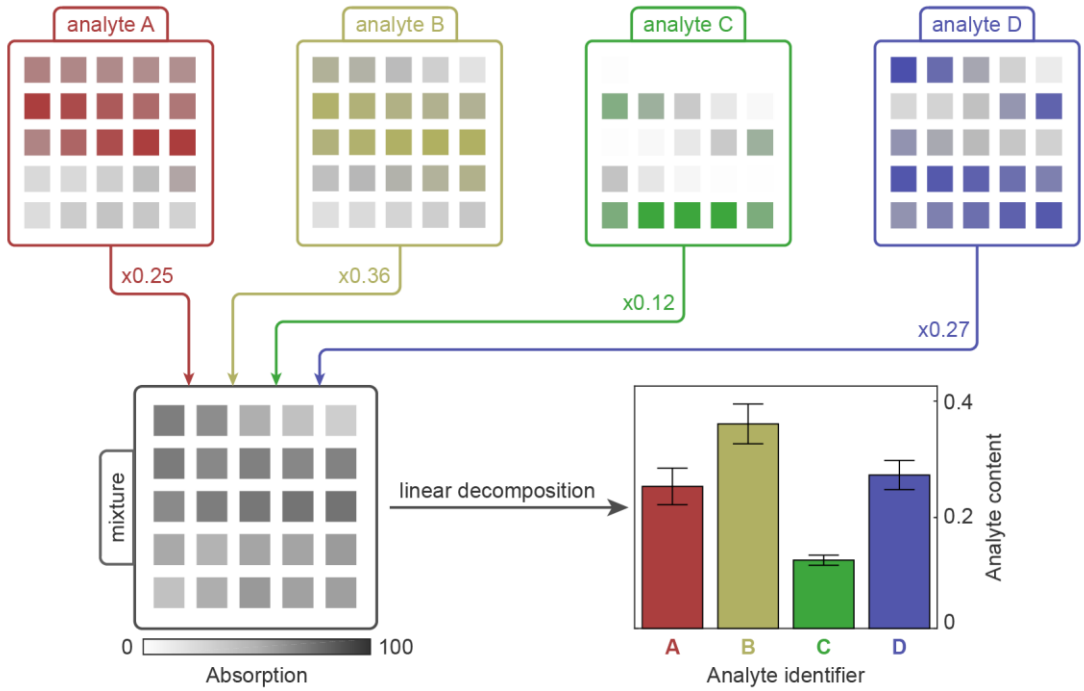

Fig. S10

Multi-analyte detection. Chemical identification in mixtures containing multiple analytes is enabled through linear decomposition analysis based on a library of molecular barcode signatures.